Imaging empty states on the Ge(100) surface at 12 K

M. Kuzmin,[1,2,*] J. Mäkelä,[1] J.-P. Lehtiö,[1] M. Yasir,[1] M. Tuominen,[1] Z. S. Jahanshah Rad,[1] A. Lahti,[1] M.P.J. Punkkinen,[1] P. Laukkanen,[1] and K. Kokko[1]

[1] *Department of Physics and Astronomy, University of Turku, FI-20014 Turku, Finland*

[2] *Ioffe Physical-Technical Institute, Russian Academy of Sciences, St. Petersburg 194021, Russian Federation*

Understanding of bias-dependent scanning-tunneling-microscopy (STM) images is complicated by not only multiplicity of the surface electronic structure but also manifold tunneling effects in probing semiconductor surfaces having directional dangling- and covalent-bond orbitals. Here we present a refined interpretation of empty-state STM images from the model semiconductor surface, Ge(100), on the basis of measurements at low temperature (12 K) combined with density functional theory calculations. In the lower-bias regime (≤1.6 V), the electron tunneling is found to occur predominantly to antibonding dangling-bond or/and dimer-bond states (π_1*, π_2*, and σ*) of Ge(100) at the surface-parallel wave vector $k_{\parallel}$=0, leading to the tunneling current maxima located directly on the dimer rows. At higher biases (e.g., at 2 V), the current maxima are shifted to the position in the troughs between the dimer rows, because the tunneling occurs efficiently to the π_2* states at $k_{\parallel}\neq 0$ associated with the dimer-up atoms of two adjacent dimer rows, i.e., because of increased sideway tunneling. Thus, the empty-state STM images of Ge(100), albeit strongly bias-dependent, reflect the dimer arrangement rather than the back bonds and surface resonances at all experimental conditions used. The results are also discussed in comparison with the counterpart system of Si(100).

I. INTRODUCTION

Due to significant fundamental and technological importance, the (100) surface of silicon has been extensively studied as the model semiconductor system.[1,2] Although the electronic structure of this surface is thoroughly described (e.g., Ref. 3 and references therein), the

interpretation of its scanning tunneling microscopy (STM) images has been a challenge for long. In particular, one of the most puzzling problems was the symmetrical view of Si topmost-layer dimers at room temperature (RT), while it was well known that such dimers are buckled (tilted) in reality.[4] Now this paradox is well understood in terms of so-called flip-flop motion (fluctuation) of Si dimers at RT, leading to an average of two tilting configurations on the time scale of STM image acquisition.[5,6]

Another challenging issue has been the strong dependence of STM images on the bias voltage and attribution of surface states found by scanning tunneling spectroscopy (STS) to electronic-state bands identified with angle-resolved photoelectron spectroscopy (ARPES) and density-functional theory (DFT) calculations.[2,7-15] Since the filled π-like and empty π*-like surface states are associated with the partial charge transfer occurring from the lower to upper atom of the buckled Si dimer and localized on the dangling bonds of these atoms, one could expect that the π and π* states can be simply viewed as dimers in filled and empty state images at RT, respectively. In fact, such an idea was employed in interpreting STM observations in earlier studies.[2,7] However, this concept does not allow one to answer at least two important questions, *i*) why the dimers are observed as bean-shaped features in filled states instead of protrusion-type entities in empty states, and *ii*) why the buckling of dimers in empty states is not seen when the dimers are pinned by defects, in disagreement with calculations.[8,9] Qin and Lagally[10] and Hata *et al.*[11] have independently reconciled these disagreements and shown that probing the π and π* states requires low biases just below and above the surface tunneling gap, and that at higher biases the main part of tunneling current comes from the states other than the π and π* states, making STM images strongly bias-dependent. Various interpretations have been proposed for these higher-energy states, including the σ*-type dimer-bond state,[11-13] the backbond state localized on the dimer up atom,[11,14] and bulk states and surface resonances (Ref. 15). These results are summarized in a diagram (the bottom half of Fig. 1) illustrating schematically energy (or sample bias voltage) ranges where different electronic bands contributing STM images of Si(100) have been identified in previous studies.

As for the counterpart of Si(100), the Ge(100) surface is significantly less understood. Despite a similarity of atomic structures of the two surfaces, the electronic structure of Ge(100) is rather different from that of Si(100), and therefore, the knowledge of the latter cannot be

directly translated to the case of Ge(100). As remarked in Ref. 3, one of such differences is the character of the valence band top (VBT) of these surfaces. While the top and bottom of valence and conduction bands on the Si(100) are exclusively the π and π^* states, the VBT of Ge(100) is not solely the π band. The *n*-type Ge(100) VBT is located only ~0.1 eV below the Fermi level (E_F), causing its strong pinning in the surface band gap, and the origin of this pinning has been widely debated recently.[3,16-19] Because of the above complexity of VBT, the view of filled states in STM images of Ge(100) is strongly influenced by the bias voltage in the range of -0.6 to -0.1 V.[20] At -0.1 V the images show up double-lobe features instead of bright protrusions which are observed at -0.6 and -0.4 V and centered on the Ge dimer-up atoms. In Ref. 20, these double-lobe features are assigned, based on DFT calculations, to the back bond surface states associated with the Ge dimer atoms, while the dangling-bond surface states were reported ~0.35 eV lower in energy (see the top half of Fig. 1). Such interpretation, however, is doubted in Ref. 21, since the result is shown to be qualitatively affected by the number of atomic layers in the slab model used for simulating the VBT. According to Ref. 21, the VBT of Ge(100) is a bulk state, in agreement with more recent studies (Refs. 3 and 19). The VBT at the *J* symmetry point of the surface Brillouin zone (SBZ) is interpreted as a surface resonance at ~0.1 eV below the Fermi energy, and this state, together with the mixed state between the dangling bond π state and the bulk state at ~0.2 eV below E_F, can explain, in particular, the experimentally observed STS feature at -0.1 V reported by Gurlu *et al*. (Ref. 22) . Thus, the interpretation of filled-state STM images of Ge(100) is rather complicated and not merely analogous to the case of Si(100).

The understanding of Ge(100) electronic structure above E_F is even more challenging, although such knowledge is very crucial for studying various physical phenomena, such as the adsorption, film growth, and current transport to a semiconductor. In particular, one of the reasons why this issue is not yet resolved enough is that probing the electronic structure above E_F requires inverse photoelectron spectroscopy which is relatively rare and demanding method in contrast to ARPES used for studying the electronic structure below E_F. Moreover, there are so far only few investigations discussing the origin of empty-state STM images from this surface[22-25] and their detailed interpretation is still lacking. The electronic structure above the Fermi level, which is the platform for understanding STM data, has been previously examined in several studies.[22,23,26-31] Using STS, Gurlu *et al*.[22] have revealed two states at 0.5 and 0.8 eV above E_F

and assigned those to dimer π^* and σ^* antibonding orbitals, respectively. Based on DFT calculations, Schwingenschlögl and Schuster[26] have reported four unoccupied states at 0.2, 0.4, 0.6, and 0.7 eV, the three lowest of which are assigned to the π^* bands and the highest to the σ^* band on the Ge(100). Tomatsu *et al*.[27] have found the π^* state at ~0.1-0.15 eV and a mixture of π^* and σ^* states at ~0.8 eV above E_F, whereas Randy *et al*.[20] have demonstrated the π^* states lying within the energy window of 0-1.0 eV above E_F. These results are summarized in Fig. 1. In addition, the π^* band has been probed by inverse photoemission[28,29] and ARPES using thermal excitation of electrons into the respective state (Refs. 30 and 31). In particular, Eriksson *et al*.[31] have reported, based on temperature-variable ARPES, the π^* band at 0.13 eV above E_F at the Γ symmetry point of SBZ. Thus, the previous results demonstrate that empty orbital STM images of Ge(100) should be contributed by several states and their detailed understanding is important to realize the fundamental similarities and differences of Ge(100) and Si(100) and predict the behavior of various adsorbates on these surfaces.

In this paper, we have refined the interpretation of electronic structure and atomic geometry of the Ge(100) surface by combining STM, STS, current imaging tunneling spectroscopy (CITS) measurements at 12 K, and DFT calculations. This combination is powerful especially because experimental results obtained at very low temperatures can be quite straightforwardly compared to DFT data corresponding to 0 K. The $c(4\times2)$ reconstruction, which is the ground state of Ge(100), is observed below 150 K and reversibly changes into the $p(2\times2)$ structure when electrons are injected from a negatively biased tip to the unoccupied states on this surface.[24,25] For this reason, we mostly deal with the $p(2\times2)$ in this study. The energy difference of $c(4\times2)$ and $p(2\times2)$ is only a few meV/dimer, and these structures are closely related to each other: both have the Ge dimers buckled in the antiferromagnetic way, but the buckling in the adjacent dimer rows is out of phase in the $c(4\times2)$, while all dimers are buckled in phase in the $p(2\times2)$. Anyway, this minor difference can cause rather significant distinctions in STM images, as will be seen below.

II. EXPERIMENTAL AND CALCULATIONAL DETAILS

All the measurements were carried out in the Scienta Omicron Fermi SPM microscope operating in the temperature range of 10-300 K. The base pressure was below 1×10^{-10} mbar. The Ge(100) samples (*n*-type, Sb-doped, ~1×10^{19} cm^{-3}) were cleaned by the standard procedure, i.e., repeated cycles of Ar ion bombardment (1.0 keV) at 400°C and subsequent annealing at 630°C until an atomically flat and clean surface was verified at RT. Then the samples were transferred to the STM housing and cooled down to 12 K with liquid helium. In all measurements the temperature of the sample was kept at 12 K and the STM scanner head at 20 K. The STM images were acquired in the constant current mode. STS and CITS measurements were performed simultaneously with the topography measurements. More details can be found in Sec. III. The WSxM package[32] was used in part for processing the data.

The calculations were performed by using Vienna *ab initio* simulation package (VASP),[33-36] applying the projector augmented wave (PAW) method[37,38] and the Perdew-Burke-Ernzerhof (PBE) generalized gradient approximation. The atomic structure was optimized by using conjugate-gradient minimization of the total energy with respect to the atomic coordinates. The plane wave cutoff energy was 350 eV. The details of STM simulations are described in Section III.

III. RESULTS AND DISCUSSION

The present findings reasonably agree with the results of Takagi *et al.*[24,25] showing that the c(4×2)↔p(2×2) phase transition induced by carrier injection using an STM occurs on the Ge(100) with hysteresis in the sample voltage bias range $-0.7 \leq V \leq 0.6$ V. An atomic resolution STM image of the c(4×2) structure at the -0.6 V bias is shown in Fig. 2a. The tunneling current (I_t) is 2.0 nA and the scanning area 10×10 nm. In this image each maximum of tunneling current is due to π dangling-bond states of two neighboring dimer-up atoms in the adjacent dimer rows. The large-scale c(4×2) structure still persists upon changing the bias polarity and increasing the voltage up to 0.8 V (Fig. 2b), however, the STM image has changed dramatically in unoccupied orbitals. The change can be clearly evidenced from the bias-reverse image presented in Fig. 2c. The scanning was performed from the bottom to the top, and the first (lower) half of the image was taken at V = -0.6 V. At the line marked by arrows the sign of bias voltage was reversed and

the second (upper) half was taken at 0.6 V. By looking at the rows of STM features running from the bottom to the top of Fig. 2c, it can be seen that the current maxima, i.e., most prominent protrusions in the filled states are replaced by the current minima, i.e., depressions in the empty states (such features are marked by symbols 'x'). Also, the current minima in the filled states are replaced by the current maxima in the empty states (shown by symbols 'o'). This behavior means that the spatial distributions of state density extremes in occupied and unoccupied orbitals are completely out of the phase. As already remarked, the c(4×2) structure is unstable against the increasing of bias voltage at $V > 0.8$ V, and thus the reliable results cannot be acquired for this structure above 0.8 V. For this reason, further we will focus on the $p(2\times2)$ for examining the empty states on the Ge(100).

At $V \geq 0.8$ V, the $c(4\times2)$ structure eventually transforms into the $p(2\times2)$, although the former can still be locally pinned by defects etc., as shown by arrow in Fig. 3a. After such transition, the $p(2\times2)$ can be also observed at $V < 0.8$ V. The view of dimer rows of this structure in empty states is clearly affected by the bias voltage. STM images taken from the same area (5.7 × 10 nm) as function of bias voltage are presented in Figs. 3b-3d. At 0.3 V the dimer rows appear as zigzag chains where individual protrusions cannot be clearly resolved. At 0.8 V the chains tend to have a less zigzag character, leading to nearly straight lines. Finally, at 1.6 V, the dimer rows exhibit the zigzag-like shape again, with individual protrusions being much better resolved as compared to the zigzag chains at 0.3 V. It is even more important that the zigzag chains at 0.3 and 1.6 V are seen to be completely out of phase, i.e., the tunneling current maxima observed at the two experimental conditions have different origins. The symbols 'x' and 'o' illustrate the tip positions where the zigzag chain observed at 0.3 V in Fig. 3b has tooth and dent, respectively. In contrast, at 1.6 V (Fig. 3d), the position 'o' corresponds to the STM protrusion, while the position 'x' corresponds to the dent of zigzag chain. Also, it is unlikely that the nearly straight lines at 0.8 V (Fig. 3c) are just a mixture of two out-of-phase chains at 0.3 and 1.6 V; otherwise, such combination would demonstrate rows of dimerized features composed of two types of protrusions. Thus, several (at least, three) surface states are probed in the STM images of Fig. 3b-d, which lie at different energies above the Fermi level and are localized on the Ge dimer rows.

The above results can be understood on the basis of simulated STM images. Prior to such an analysis, we briefly discuss some aspects of probing unoccupied states in STM. According to STM theories,[39-43] the tunneling current can be written as $I_t \propto \int_0^{eV} \rho_{sub}(E)T(E,eV)dE$, where $T(E,eV) = e^{-2\kappa s}$ is the transmission probability of the electron, $\kappa = \sqrt{\frac{2m}{\hbar^2}\left[\frac{\left(\phi_{tip}+\phi_{sub}\right)}{2} - E + \frac{eV}{2}\right] + k_{\parallel}^2}$ is the inverse decay length, s is the distance from the tip to the sample, E is the energy of the surface state relative to E_F, ϕ_{tip} and ϕ_{sub} are the work functions of the tip and the substrate, respectively, $\rho_{sub}(E)$ is the local density of states (LDOS) of the substrate, and $k_{\parallel}$ is the surface-parallel component of the wave vector for an electron. Here the LDOS of the tip is assumed to be featureless, which is a good approximation for typical tungsten tips. It can be seen that in empty orbitals ($V > 0$) the maximum transmission probability occurs for electrons tunneling to the surface states at $E = eV$, i.e., $T(E, eV) \leq T(eV, eV)$. Figure 4 examplifies the normalized transmission probability, $T(E, eV)/T(eV, eV)$, as function of the energy of an unoccupied state (E) probed with the constant bias voltage $V = 2$ V. This calculation is made at the Γ point of SBZ ($k_{\parallel} = 0$) for the typical experimental parameter $(\phi_{tip}+\phi_{sub})/2 = 4.5$ eV. As seen in Fig. 4, the transmission probability essentially lowers with decreasing the energy of probed state. In particular, $T(E)$ is reduced by 23%, 40%, and 52% at $E = 1.5$, 1.0, and 0.5 eV, respectively, as compared to the transmission probability at $E = 2.0$ eV. Therefore, strictly speaking, STM simulations should be performed by integration of LDOS weighed by the above considered exponential tunneling factor. In this work, however, we simplified STM simulations, which is sufficient for unveiling the general tendencies in empty-state STM images of Ge(100)p(2×2) with the variation of bias voltage. Namely, instead of introducing the tunneling factor, we integrated the surface LDOS in different energy ranges in our STM simulations. In particular, contour maps of constant surface LDOS are obtained by integration within two types of energy windows: (*i*) from $E_{MIN} = E_F = 0$ to eV and (*ii*) from $E_{MIN} > 0$ to eV. It is worthwhile noting that such approach allowed us to reveal the common trends in comparable calculations and measurements, and that a one-to-one correspondence of calculated and measured images should be hardly expected in any case. One of the reasons, for instance, is the well-known problem of underestimating the band gap in DFT calculations.

Some of the simulated images, which are 2D maps of the LDOS, or the charge density of the sample states, are presented in Fig. 5. The superimposed large and small solid circles show the positions of the dimer-up and -down atoms, respectively. In the low-bias regime (the energy range 0-0.6 eV) the most prominent state density is localized on the dimer-down atoms and can be attributed to the π^* dangling bond state. Such features appear in the form of round protrusions arranging characteristic zigzag chains, in a good agreement with experiment [V = 0.3 V (Fig. 3b)]. In addition, there is very small weight of the LDOS near the dimer-up atoms, which appears in the form of small spurs and is difficult to be resolved in experiment. The LDOS between the dimer-down and –up atoms is still relatively high.

When the LDOS integration is performed within the energy windows of 0-0.8 eV and 0.6-1.0 eV, the prominent feature, which is associated with the π^* state and located the down atoms, is still present, but another LDOS maximum localized on the dimer-up atom starts to develop. This maximum becomes dominant in the energy window of 0.8-1.6 eV. Thus, the DFT calculations reveal that the highest state density is moved from the position above the dimer-down atom at lower energies (below 0.6 eV) to the position above the dimer-up atom at the energies of 0.8-1.6 eV, which is fully consistent with experiment (Fig. 3). In particular, such behavior can explain the observation of out-of-phase zigzag chains at 0.3 and 1.6 V in Fig. 3.

Interestingly, there is no LDOS minimum between the dimer-up and -down atoms in the energy ranges of 0-0.6 eV and 0-0.8 eV in Fig. 5, while such minima clearly appear in those of 0.6-1.0 eV and 0.8-1.6 eV, leading to a dark, slightly meandering, river flowing along the longer axes of dimer rows. This infers that there is another state contributing to STM images at $E \leq 0.8$ eV, in addition to the π^* state. This additional state is located near the center of dimer and can also appear as a small spur seen in the simulated image at 0-0.6 eV. A possible candidate for such a state is the antibonding σ^* dimer-bond state. Its existence can account for why the experimental protrusions along the dimer rows at the bias voltages of 0.3 and 0.8 eV are not resolved (Figs. 3b and 3c), in contrast to those at 1.6 eV (Fig. 3d). Furthermore, the significant contribution of the σ^* state to the tunneling current at the bias voltage of 0.8 V (Fig. 3c) can explain the appearing of dimer rows in the form of nearly straight lines.

A comparison of results for the two types of LDOS integration in Fig. 5 reveals that the charge density contours simulated in the case of $E_{MIN} > 0$ are in better agreement with experiment than those at $E_{MIN} = 0$. For example, as shown in the right panel of Fig. 5, the image simulated within the energy range of 0.8-1.6 eV gives rise to well-defined zigzag chains composed of individual, well resolved, protrusions, while the image obtained within the 0-1.6 eV range shows rows composed of dimerized features rather than zigzag chains. Clearly, the former image reasonably reproduces the measured one at $V = 1.6$ V (Fig. 3d), whereas the latter is fully inconsistent with the measurements. Obviously, the above difference can be well understood in terms of the results presented in Fig. 4. Calculated STM images at higher energy will be considered below.

An important similarity of experimental and simulated STM features at $V \leq 1.6$ V in Figs. 3 and 5 is that the maxima of state density and tunneling current are always observed when the tip is located over the dimer rows, whereas dark channels are seen whenever the tip is located in the troughs between the dimer rows. Our results show that this is not the case for higher bias voltages. Figure 6 presents a dual-bias image of which bottom part is taken at $V = 1.5$ V and top part at 2.0 V (the bias voltage is instantly changed from 1.5 to 2.0 V at the line shown by arrows). It is seen that after the bias increase, the current maxima are no longer observed for the tip on the dimer rows but in the troughs. Especially, the difference is evident for the local $c(4\times2)$ structure where the STM protrusions at 2.0 V are located in between two neighboring up atoms of adjacent dimer rows. In principle, the above shift of the current maxima might suggest an additional state that is located in the troughs. Its energy is higher than 1.6 eV so that the state cannot be probed at $V \leq 1.6$ V. Such explanation, however, is questionable in light of DFT results in Fig. 5 which do not support the additional state in the troughs (see the simulated image at 1.6-2.0 eV). Moreover, our calculations reveal no state in the troughs up to 3 eV (not shown here). With increasing the energy in simulated STM images one can see only a slight shift of state density maxima located on the upper atom toward the troughs. However, this small change cannot account for the qualitative change in the experimental image of Fig. 6.

Alternatively, another explanation can be proposed. It is usually considered in the analysis of STM data that only the states at the Γ symmetry point of SBZ, i.e., at $k_{\parallel} = 0$ contribute to the tunneling current, and the contribution of states at $k_{\parallel} \neq 0$ is postulated to be

negligible. This assumption is based on the fact that the inverse decay length is dependent on $k_{\parallel}$, and therefore, the state located at Γ is expected to have a larger contribution to the tunneling current than the state with a non-zero parallel momentum.[43,44] Here our analysis indicates that the above assumption is not always valid, and that the contribution of states at $k_{\parallel} \neq 0$ should not be underestimated in the STM analysis. Moreover, the tunneling to states at $k_{\parallel} \neq 0$ can even overwhelm the tunneling to states at $k_{\parallel} = 0$ in some cases. It should be noticed that the influence of the geometry and tip shape on the tunneling current was first investigated by Garcia *et al*. in the early 1980s.[45] In the present study, the role of states at $k_{\parallel} \neq 0$ is elucidated by considering how the transmission probability decreases with the angle θ between the surface normal and the direction along which an electron is tunneling from the tip to a surface state (see in the inset in Fig. 7). Taking into account that $k_{\parallel}^2 = \frac{2m}{\hbar^2} E_{kin} \sin\theta^2$ (E_{kin} is the kinetic energy of electron), the inverse decay length can be presented as function of angle θ in the form $\kappa(\theta) = \sqrt{\frac{2m}{\hbar^2}\left[\frac{\left(\phi_{tip}+\phi_{sub}\right)}{2} - E + \frac{eV}{2} + E_{kin}\sin^2\theta\right]}$. Note that the energy E in this equation can be also dependent on θ if the respective electronic state disperses with $k_{\parallel}$. For sake of simplicity, here we consider the dispersionless state, and then one can obtain the θ dependence of transmission probability as $T(\theta) = e^{-2\kappa(\theta)s/\cos\theta}$. Using such approach, the normalized transmission probability, $T(\theta)/T_0$, can be plotted as function of θ, where $T_0 = T(0)$ is the transmission probability at $\theta = 0$ ($k_{\parallel} = 0$). In Fig. 7 we illustrate two such dependences for typical experimental parameters $(\phi_{tip} + \phi_{sub})/2 = 4.5$ eV and $E = eV = 1$ and 2 eV. On the basis of Fig. 7, considering the SBZ of Ge(100)p(2×2) (0.787 × 0.787 Å^{-1}), $T(\theta)/T_0$ can be quantified at some symmetry points of k-space far from the Γ point. Table I presents the normalized transmission probability at the ½×ΓJ, ½×ΓK, J, and K symmetry points at $E_{kin} = 1$ and 2 eV. It is seen that the states far from the middle of SBZ can provide an important contribution to the tunneling current, and that their role becomes more significant with the energy, leading to increased *sideway* tunneling. Also, if the empty state disperses with the parallel momentum upward, $T(\theta)/T_0$ decreases with the angle θ even more slowly, and the role of states with a non-zero $k_{\parallel}$ becomes more important. Moreover, the current distribution can even have a maximum for non-zero θ. In fact, while the $T(\theta)$ decreases with θ, the number of tunneling electrons between the angles θ and $(\theta + \Delta\theta)$ increases due to the increased solid angle $2\pi \sin\theta\, \Delta\theta$, which

in principle can result in non-monotonous angle-dependence of the tunneling current. Thus, we assume that the tunneling current maxima in STM image measured at 2 V in Fig. 6 are not necessarily due to the states located in the troughs directly.

Further, the origin of states probed at 2 V and shift of zigzag features in Fig. 6 can be elucidated by CITS. Here, along with a topography image acquired in the constant current mode, current-voltage (*IV)* curves are recorded at demanded points of the image. In our study the topography image is measured at $V = 1.5$ V and $I = 0.2$ nA (the feedback loop on) and includes 400 × 400 datapoints. At every third datapoint along every third scanning line the STM tip is stopped, the feedback loop disabled (at the chosen tunneling current), and the bias voltage swept out for measuring an *IV* curve shortly. Because of a short period of the *IV* measurement, the tip drift is neglected. Finally, the feedback is reactivated for further measurements. As a result, a set of *IV* curves is collected, and then these data can be transformed into current images (134 × 134 pixels each) at constant bias voltages. In addition, $(dI/dV)/(I/V)$ images can be also obtained by numerical differentiation. Figure 8 shows a set of selected current images for different bias voltages together with the topography image from the $p(2\times2)$ structure. The vertical dot lines are just for eye. It is seen that around $V = 1.5$ V the current image shows fully uniform background without any features. This is because the tunneling current is set to be constant at this bias voltage, and indeed such stabilization is confirmed by CITS. At lower and higher voltages the current images are no longer uniform. At $V = 1.44$ V and lower the maxima of tunneling current occur for the tip over the dimer rows, and at V = 1.58 V and higher those occur for the tip in the troughs. The line profiles taken along the horizontal line in the topography image clearly illustrates this registry shift in the current images around 1.5 V (at bottom of Fig. 8). At the same time, our DFT simulations do not reveal any significant LDOS in the troughs, which could contribute to the tunneling current substantially. Based on these CITS and DFT data, we conclude that the lateral shift of tunneling current maxima at 2.0 V in Fig. 6 is not due to an appearing of additional states in the troughs. We assume that at this bias voltage the electrons can be easily injected from the tip located in the trough to unoccupied states localized on two neighboring dimer rows, leading to the maximum of tunneling current across the images. Note that the injection of electrons to states at $k_{\parallel} \neq 0$, i.e., sideway tunneling becomes more probable with increasing the energy and bias voltage so that the lateral shift of current maxima is bias-

dependent. In contrast, at $V \leq 1.5$ V the highest tunneling current occurs when the tip is over the dimer row and electrons are injected to states at $k_{\parallel} = 0$.

More information about unoccupied surface states on the Ge(100)p(2×2) can be gained by examining the electronic structure by STS. Figure 9 shows a dI/dV spectrum averaged over the defect-free p(2×2) area. The tunneling gap is rather limited (~0.1 eV) and, as seen in the inset of Fig. 9, there is the non-zero DOS just below or even crossing the Fermi level. This is in well agreement with earlier studies that reported an occupied state exactly in the same energy range, which makes strong Fermi level pinning at 0.1 eV above VBM for *n*-Ge.[3,16-19]

The local surface electronic structure above the Fermi level can be studied with normalized conductivity (dI/dV)/(I/V) curves providing an idea about the state energy and density. Figure 10 shows two curves obtained for two different STM tip positions: on the dimer row and in the trough. Each of the curves is an average of several spectra taken at different points of defect-free *p*(2×2) surface. Before we proceed with the analysis, it is worth noting that the (dI/dV)/(I/V) data acquired from different parts of the dimer row (e.g., on the lower and upper dimer atoms, the dimer bond etc.) are found to be rather similar. This similarity can derive from that the respective unoccupied states are delocalized or/and the states at $k_{\parallel} \neq 0$ significantly contribute to the tunneling current in addition to those at $k_{\parallel} = 0$. As seen in Fig. 10, the most prominent features of the (dI/dV)/(I/V) spectrum measured on the dimer row are sharp peaks, S_1 and S_2, at 0.24 and 0.70 eV, respectively, as well as a shoulder (S_3) at 0.88 eV. Similar features are also found for the spectrum measured in the trough. Their energies, however, are systematically slightly shifted toward the higher binding-energy side (0.28, 0.79, and 1.07 eV, respectively). Moreover, the intensities of these features are lowered when the tip is located in the trough. On this basis, we assume that the S_1, S_2, and S_3 are localized on the dimer row. Their energy shifts can be explained by energy dispersions of respective surface-state bands (see below).

Likewise, there is a qualitative similarity of spectra in Fig. 10 in the higher bias-voltage range (1.3-2.0 V). Namely S_4 and S_5 features are identified for the both spectra, and the corresponding states can be probed at both positions of STM tip as well. These features, however, are more pronounced for the STM tip in the trough, in contrast to the S_1-S_3 states. Also, the binding energies of S_4 and S_5 are 1.51 and 1.64 eV when the tip is in the trough, and 1.54 and

1.72 eV when the tip is on the dimer row. This behavior is opposite to that of S_1-S_3. Using the same arguments discussed above, we assume that the S_4 and S_5 are localized in the troughs.

The $(dI/dV)/(I/V)$ data in Fig 10 are found to agree well with the calculated band structure for the Ge(100)p(2×2) surface. In Fig. 11 we present the electronic structure of this surface calculated above the Fermi level. The dimer row direction is shown by arrow. Among the electronic bands in Fig. 11, the lowest surface-state band [the binding energy is 0.03 eV at the Γ symmetry point of p(2×2) SBZ] and second lowest one (0.35 eV at the Γ) have the highest degree of localization. Both are mostly localized on the dimer-down atoms. Also, the both bands disperse upward along the dimer rows (i.e., along $\Gamma - J'$ and $J - K$) and are almost dispersionless in the perpendicular direction (i.e., along $\Gamma - J$ and $K - J'$), that is, these bands have a one-dimensional character. The other bands are significantly more delocalized and have a more two-dimensional character. Here we focus on four bands at 0.77, 1.17, 1.23, and 1.31 eV at the Γ (shown by thicker solid lines in Fig. 11). The former two are found to have approximately equal weight on the dimer-down and –up atoms, while the weight of the latter two is higher on the dimer-up rather than dimer-down atoms. Based on these findings as well as the results in Figs. 3, 5, and 10, we can attribute the S_1 feature in Fig. 10 and the electronic bands at 0.03 and 0.35 eV at the Γ in Fig. 11 to the π_1* dangling-bond orbital. It is mostly localized on the dimer-down atom and significantly contributes to the tunneling current at the bias voltage as low as 0.3 V (Fig. 3b). The respective feature also appears in DFT calculations in the form of round protrusion in the energy windows 0-0.6, 0-0.8, and 0.6-1.0 eV in Fig. 5. Next, the S_2 and S_3 features in Fig. 10 and four bands in the 0.77-1.31 eV energy range at the Γ in Fig. 11 are assumed to be due to a mixture of the antibonding σ* dimer-bond and π_2* dangling-bond orbitals. The contributions of such states to STM images are evident at the bias voltages of 0.8 and 1.6 V (Figs. 3c and 3d). Most likely, the σ* state significantly contributes to the tunneling current at 0.8 V, leading to nearly straight lines instead of zigzag features in the STM image. Hence, the S_2 can be attributed to the σ* state. Probing the π_2* state is possible at higher biases; as seen in Fig. 3d as well as Fig. 5 the contribution of this state becomes dominant at 1.6 V and it is localized near the dimer-up atom. Therefore, the S_3 can be attributed to the π_2* one. Similarly, we assume that the bands at 0.77 and 1.17 eV at the Γ in Fig. 11 have predominantly the σ* character and those at 1.23 and 1.31 eV the π_2* character. Thus, our results reveal at least two unoccupied surface-state bands

(π_1* and π_2*) associated with the dimer dangling-bond orbitals. These bands are separated in energy and respective surface states have different spatial distributions: the lower-energy one, π_1* (S_1), is mostly located on the dimer-down atoms and the higher-energy one, π_2* (S_2), on the dimer-up atoms.

The assignment of S_4 and S_5 is much more complicated. First of all, these states are not as pronounced as the $S_1 - S_3$ ones. Second, no states, which could provide a notable contribution to STM images, are identified in the troughs by DFT calculations. Thus, it is unlikely the S_4 and S_5 can be probed in a pure form at 2 V in Fig. 6, where their contribution to the tunneling current can be overwhelmed by the π_2* states. Taking into account the binding energies and spatial distribution of S_4 and S_5, we assume that these features can be related to the backbonds of the dimer-up atoms or/and bulk states. The above results not only provide the refined interpretation of electronic structure of Ge(100) studied earlier in Refs. 22, 23, and 26-31 but also offer a good platform for understanding the strongly bias-dependent empty-state STM images from this surface. Moreover, we notice that the approach considered here opens a way to study the $k_{\|}$ dependences of unoccupied surface-state bands with STS.

Finally, we briefly compare the STM data for Ge(100) and Si(100) surfaces. In the context of this study, it should be noticed that both surfaces show very common trend in empty-state STM images: namely a similar lateral shift of tunneling current maxima in the direction perpendicular to the dimer rows is observed on the Si(100) in increasing the bias voltage.[10-15] In the case of Si(100), however, such a shift has been interpreted in different ways. While there is the consensus concerning the origin of zigzag chains in the lower-bias images (i.e., it has been proposed that they are due to tunneling to π* states associated with the buckled Si dimer), the origin of STM features at the higher biases is still under debate. Qin and Lagally[10] have suggested that the higher-bias empty-state images of Si(100) (e.g., at 2.0 V) are not predominantly determined by the surface dangling-bond state, reflecting mixed states, with the surface state contribution not prominent. Hata *et al.*[11] proposed that the back bond and dimer bond states are probed by STM at the high-bias voltages (≥1.5 V). Also, in the study of Si(100)p(2×2) at 40 K, Hata *et al.*[15] found that STM images at 1.5 V do not reflect the surface structure because tunneling to bulk states and surface resonances overwhelm tunneling to the π* states. Finally, Okada *et al.*[12] and Nakayama *et al.*[13] reported the π_2* and σ* states to be probed

at biases of 1.2-2.0 and ≥2.1 V, respectively, while Perdigão *et al.*[14] found, by probing the Si(100) at 5 K, the back bond state at 1.5 eV. In the present study, however, we found that neither back bond nor bulk states/surface resonances are responsible for mapping in STM and current images on the Ge(100)$p(2\times2)$. At the low biases (≤1.6 V), the π^*- and σ^*-type states at $k_{\|} = 0$ are mostly probed in STM images, leading to zigzag chains or nearly straight lines which are localized directly on the dimer rows. At the higher biases (2 V), the shift of tunneling current features, i.e., an appearing of zigzag chains of STM images in the troughs between the dimer rows, is due to sideway tunneling to π_2^* states. Such states are localized on two neighboring dimer rows adjacent to the tip located in the trough. In Fig. 1, we summarize these results and compare them with previous observations.

In addition, it is worthwhile noting that for the Si(100) surface, the symmetric-dimer STM images and apparent $p(2\times1)$ periodicity have been observed after cooling below ~20 K, [46,47] and their origin has been extensively discussed (e.g., see Ref. 48 and references therein). In contrast, no symmetrical-dimer STM images are revealed for the Ge(100) surface at 12 K in this study. This implies another important difference between the two surfaces.

IV. CONCLUSIONS

In this study, the refined interpretation of empty-state STM images from the Ge(100) surface is presented on the basis of STM, STS, and CITS measurements at 12 K combined with DFT calculations. It is shown that the images are strongly bias-dependent, and that in the low-bias range (0.3-0.8 V) they are contributed by the π_1^* or/and σ^* states. The former state is found at 0.24 eV [at the Γ symmetry point of the $p(2\times2)$ SBZ] above the Fermi level and localized mostly on the down atoms of buckled Ge dimers, resulting in the zigzag chains in the STM image at 0.3 V. Such chains are centered on the dimer rows of the $p(2\times2)$ reconstruction. The latter state is found at 0.70 eV at the Γ; its strong contribution to STM images is observed at 0.8 V where the dominant features of the respective image are nearly straight lines centered on the longer axis of dimer rows. The third state contributing significantly to empty-state STM images is the π_2^* state which lies at 0.88 eV (at the Γ point of SBZ) and mostly localized on the dimer-up atoms. It is predominantly reflected and clearly resolved in STM images at 1.6 V, where the

π_2* state appears in the form of individual protrusions arranged in the zigzag manner. The contributions of π_1* and σ* states are rather small at these experimental conditions.

While all observed STM features are centered directly on the dimer rows in STM images at ≤1.6 V, the maximum of tunneling current at higher biases is laterally shifted in the direction perpendicular to the dimer rows. At 2.0 V the current maximum occurs when the tip is in the trough between the dimer rows. Our results indicate that such behavior is due to sideway tunneling to the π_2* states at $k_\parallel \neq 0$, which are associated with two adjacent dimer rows. The other states, such as, e.g., the back bond states, can also give some contribution to the tunneling current, but it is rather low.

In addition to the refined interpretation of STM images and electronic structure of Ge(100)p(2×2), we have also shown that the transmission probability in the tunneling to the unoccupied surface states significantly lowers with the decrease in the binding energy of this state so that simulating STM images of Ge(100)p(2×2) requires weighed integration of LDOS with $E_{MIN} > 0$, leading to a better agreement with experiment. Also, it is found that the contribution of states at $k_\parallel \neq 0$ to tunneling current should be taken into account along with that of states at $k_\parallel = 0$. The role of sideway tunneling becomes more significant with the increase in binding energy or/and bias voltage. In some cases this might be the source of strong bias dependences of STM images where tunneling to states at $k_\parallel \neq 0$ can overwhelm tunneling to states at $k_\parallel = 0$.

ACKNOWLEDGMENTS

This work has been supported by the University of Turku Graduate School (UTUGS) and the Academy of Finland (via the project #296469).

[1] Oura, K.; Lifshits, V.G.; Saranin, A.A.; Zotov, A.V.; and Katayama, M. (2003) Surface Science: An Introduction. Berlin: Springer-Verlag. 440 p.

[2] J.A. Kubby and J.J. Boland, Surf. Sci. Rep. **26**, 61 (1996).

[3] Hosung Seo, Richard C. Hatch, Patrick Ponath, Miri Choi, Agham B. Posadas, and Alexander A. Demkov, Phys. Rev. B **89**, 115318 (2014).

[4] D.J. Chadi, Phys. Rev. Lett. **59**, 1691 (1987).

[5] R.J. Hamers, R.M. Tromp, and J.E. Demuth, Phys. Rev. B **34**, 5343 (1986).

[6] R.A. Wolkow, Phys. Rev. Lett. **68**, 2636 (1992).

[7] R. J. Hamers, Ph. Avouris, and F. Bozso, Phys. Rev. Lett. **59**, 2071 (1987); J. Vac. Sci. Technol. A **6**, 508 (1988).

[8] D.J. Chadi, Phys. Rev. Lett. **43**, 43 (1979); J. Ihm, M. L. Cohen, and D. J. Chadi, Phys. Rev. B **21**, 4592 (1980).

[9] J. Pollmann, P. Kruger, and A. Mazur, J. Vac. Sci. Technol. B **5**, 945 (1987).

[10] X.R. Qin and M.G. Lagally, Phys. Rev. B **59**, 7293 (1999).

[11] Kenji Hata, Satoshi Yasuda, and Hidemi Shigekawa, Phys. Rev. B **60**, 8164 (1999).

[12] Hiromi Okada, Yoshitaka Fujimoto, Katsuyoshi Endo, Kikuji Hirose, and Yuzo Mori, Phys. Rev. B **63**, 195324 (2001).

[13] Koji S. Nakayama, M. M. G. Alemany, Tomoko Sugano, Kenji Ohmori, H. Kwak, James R. Chelikowsky, and J. H. Weaver, Phys. Rev. B **73**, 035330 (2006).

[14] L. Perdigão, D. Deresmes, B. Grandidier, M. Dubois, C. Delerue, G. Allan, and D. Stiévenard Phys. Rev. Lett. **92**, 216101 (2004).

[15] Kenji Hata, Shoji Yoshida, and Hidemi Shigekawa, Phys. Rev. Lett. **89**, 286104 (2002).

[16] A. Dimoulas, P. Tsipas, A. Sotiropoulos, and E. K. Evangelou, Appl. Phys. Lett. **89**, 252110 (2006).

[17] T. Nishimura, K. Kita, and A. Toriumi, Appl. Phys. Lett. **91**, 123123 (2007).

[18] P. Tsipas and A. Dimoulas, Appl. Phys. Lett. **94**, 012114 (2009).

[19] Mikhail Kuzmin, Pekka Laukkanen, Jaakko Mäkelä, Marjukka Tuominen, Muhammad Yasir, Johnny Dahl, Marko P. J. Punkkinen, and Kalevi Kokko, Phys. Rev. B **94**, 035421 (2016).

[20] M.W. Radny, G.A. Shah, S.R. Schofield, P.V. Smith, and N.J. Curson, Phys. Rev. Lett. **100**, 246807 (2008).

[21] Binghai Yan, Chiyung Yam, Andreia Luisa da Rosa, and Thomas Frauenheim, Phys. Rev. Lett. **103**, 189701 (2009).

[22] Oguzhan Gurlu, Harold J.W. Zandvliet, and Bene Poelsema, Phys. Rev. Lett. **93**, 066101 (2004).

[23] J.A. Kubby, J.E. Griffith, R.S. Becker, and J.S. Vickers, Phys. Rev. B **36**, 6079 (1987).

[24] Y. Takagi, K. Nakatsuji, Y. Yoshimoto, and F. Komori, Phys. Rev. B **75**, 115304 (2007).

[25] Yasumasa Takagi, Yoshihide Yoshimoto, Kan Nakatsuji, Fumio Komori, Surf. Sci. **559**, 1 (2004); Surf. Sci. **593**, 122 (2005).

[26] U. Schwingenschlögl and C. Schuster, Chem. Phys. Lett. **449**, 126 (2007).

[27] Kota Tomatsu, Kan Nakatsuji, Masamichi Yamada, and Fumio Komori, Phys. Rev. Lett. **103**, 266102 (2009).

[28] L. Kipp, R. Manzke, and M. Skibowski, Surf. Sci **269/270**, 854 (1992).

[29] M. Skibowski and L. Kipp, J. Electron Spectrosc. Relat. Phenom. **68**, 77 (1994).

[30] C. Jeon, C. C. Hwang, T.-H. Kang, K.-J. Kim, B. Kim, Y. Chung, and C. Y. Park, Phys. Rev B **74**, 125407 (2006).

[31] P. E. J. Eriksson, M. Adell, Kazuyuki Sakamoto, and R. I. G. Uhrberg, Phys. Rev B **77**, 085406 (2008).

[32] I. Horca, R. Fernández, J.M. Gómez-Rodríguez, J. Cochero, J. Gómez-Herrero, A.M. Baro, Rev. Sci. Instrum. **78**, 013705-1 (2007).

[33] G. Kresse, J. Hafner, Phys. Rev. B **47**, 558 (1993).

[34] G. Kresse, J. Hafner, Phys. Rev. B **49**, 14251 (1994).

[35] G. Kresse, J. Furthmüller, Comput. Mater. Sci. **6**, 15 (1996).

[36] G. Kresse, J. Furthmüller, Phys. Rev. B **54**, 11169 (1996).

[37] P.E. Blöchl, Phys. Rev. B **50**, 17953 (1994).

[38] G. Kresse, D. Joubert, Phys. Rev. B **59**, 1758 (1999).

[39] J. Tersoff, D.R. Hamann, Phys. Rev. Lett. **50**, 1998 (1983).

[40] J. Tersoff, D.R. Hamann, Phys. Rev. B **31**, 805 (1985).

[41] A. Selloni, P. Carnevali, E. Tosatti, and C.D. Chen, Phys. Rev. B **31**, 2602 (1985).

[42] N.D. Lang, Phys. Rev. B **34**, 5947 (1986).

[43] R.M. Feenstra, J.A. Stroscio, and A.P. Fein, Surf. Sci. **181**, 295 (1987).

[44] J.A. Stroscio, R.M. Feenstra and A.P. Fein, Phys. Rev. Lett. **57**, 2579 (1986); R.M. Feenstra and J.A. Stroscio, "Methods of Tunneling Spectroscopy", *Scanning Tunneling Microscopy*, Ed. by W. J. Kaiser and J. A. Stroscio, San Diego: Academic Press, Inc., (1993).

[45] N. Garcia, C. Ocal, and F. Flores, Phys. Rev. Lett. **50**, 2002 (1983).

[46] Y. Kondo, T. Amakusa, M. Iwatsuki, H. Tokumoto, Surf. Sci. **453**, L318 (2000).

[47] T. Yokoyama and K. Takayanagi, Phys. Rev. B **61**, R5078 (2000).

[48] Xiao-Yan Ren, Hyun-Jung Kim, Chun-Yao Niu, Yu Jia, and Jun-Hyung Cho, Scientific Reports **6**, 27868 (2016).

FIGURE 1. (Color online) Diagram showing schematically energy (sample bias voltage) ranges where different electronic bands contributing STM images are identified for Si(100) (Refs. 10-15) and Ge(100) (Refs. 20-22, 26, and 27). In addition, the results of this study are included for comparison. They are described in Section III.

FIGURE 2. (Color online) (a.b) STM images of the Ge(100)*c*(4×2) surface at negative and positive sample-bias voltages. (a) V = -0.6 V, I_t = 2.0 nA, (b) V = 0.8 V, I_t = 0.5 nA. The scanning area is 10 × 10 nm. (c) Bias-reversed STM image of Ge(100)*c*(4×2). The bottom half is taken at V = -0.6 V and the top one at V = 0.6 V. The sign of bias voltage is reversed within the tip position marked by arrows. I_t = 2.0 nA and the scanning area is 10 × 8 nm.

FIGURE 3. (Color online) (a.b) Empty-state STM image of the Ge(100)*p*(2×2) surface at V = 0.3 V. The tunneling current is 0.5 nA, the scanning area is 10 × 8 nm. A local *c*(4×2) structure is marked by arrow. (b)-(d) Bias-dependent STM images of the same surface area (5.7 × 10 nm). The bias voltage is 0.3, 0.8, and 1.6 V, respectively. The symbols '**x**' and '**o**' represent equivalent locations on the *p*(2×2) surface.

FIGURE 4. Dependence of normalized transmission probability, $T(E, eV)/T(eV, eV)$, on the energy of a probed state. The calculation is performed at V = 2 V, $(\phi_{tip}+\phi_{sub})/2$ = 4.5 eV, and $k_{\parallel}$ = 0.

FIGURE 5. (Color online) 2D maps of the LDOS calculated for the Ge(100)*p*(2×2) within different energy windows. The large and small circles represent the position of dimer-up and -down atoms, respectively.

FIGURE 6. (Color online) Dual-bias empty-state STM image of Ge(100)*p*(2×2). The bias voltage is changed from V = 1.5 V to 2.0 V at the tip position marked by arrows. The tunneling current is 0.3 nA.The scanning area is 12.5 × 8.7 nm.

FIGURE 7. Dependences of normalized transmission probability, $T(\theta)/T_0$, on the angle θ. The calculation is performed at $E = eV$ = 1 and 2 eV and $(\phi_{tip}+\phi_{sub})/2$ = 4.5 eV. The angle θ corresponds to the case of $k_{\parallel} = 0$. The geometry of measurements is illustrated in the inset.

FIGURE 8. (Color online) Selected current images taken by CITS at V = 1.06, 1.44, 1.51, 1.58, 1.68, and 2.0 V together with constant-current topography image at V = 1.5 V. The bottom panel represents line profiles taken across dimer rows along the dashed line in the topography image and the same lines in current images at 1.3 and 1.9 V.

FIGURE 9. *dI*/*dV* spectrum of the Ge(100)*p*(2×2) surface. The spectrum is averaged over a large defect-free area. The inset shows the *dI*/*dV* curve near the Fermi level in more detail.

FIGURE 10. Normalized conductivity spectra, (*dI*/*dV*)/(*I*/*V*), taken on the dimer row and in the trough of Ge(100)*p*(2×2). The STS setpoint: V = 1.5 V, I_t = 0.3 nA. See in the text for details.

FIGURE 11. (Color online) Calculated band structure for the Ge(100)*p*(2×2) above the Fermi level. Six lowest-binding-energy electronic bands shown by thicker solid lines are contributed by π_1*, σ*, and π_2* states, and their assignments are shown. Also, the *p*(2×2) SBZ and high-symmetry points are illustrated. The dimer-row direction is pointed by arrow.

Table I. The normalized transmission probability, $T(\theta)/T_0$, at different symmetry points of the Ge(100)p(2×2) SBZ and kinetic energies of electron.

Symmetry point	$k_{\parallel}$ (Å^{-1})	E_{kin} = 1 eV		E_{kin} = 2 eV	
		θ	$T(\theta)/T_0$	θ	$T(\theta)/T_0$
1/2×□*ΓJ*□	0.197	23°	0.65	11.5°	0.85
1/2×□*ΓK*□	0.279	33°	0.40	16°	0.79
J	0.394	50°	0.07	33°	0.34
K	0.557	-	-	50°	0.05

The angle θ is calculated using the formula $k_{\parallel}(\AA^{-1}) = 0.512\sqrt{E_{kin}}\sin\theta$.

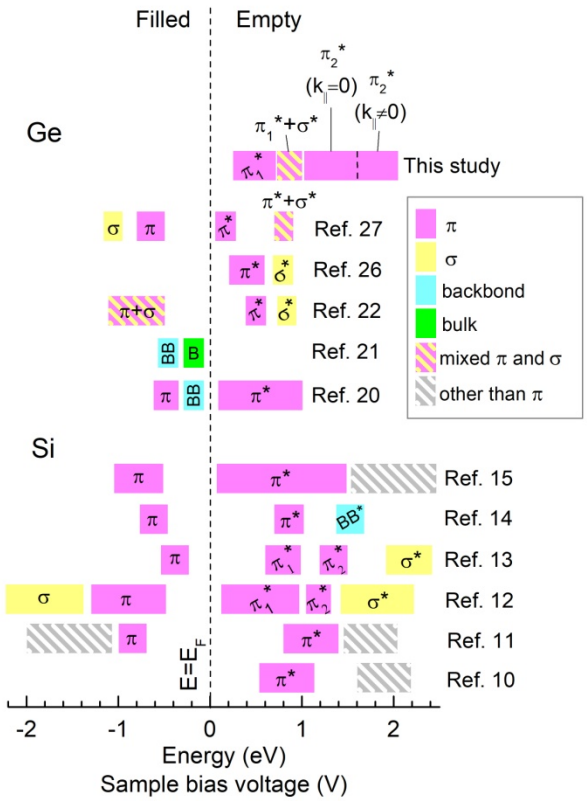
Filled
Empty
Ge
Si
This study
Ref. 27
Ref. 26
Ref. 22
Ref. 21
Ref. 20
Ref. 15
Ref. 14
Ref. 13
Ref. 12
Ref. 11
Ref. 10
π
σ
backbond
bulk
mixed π and σ
other than π
E=E_F
-2
-1
0
1
2
Energy (eV)
Sample bias voltage (V)

Figure 1

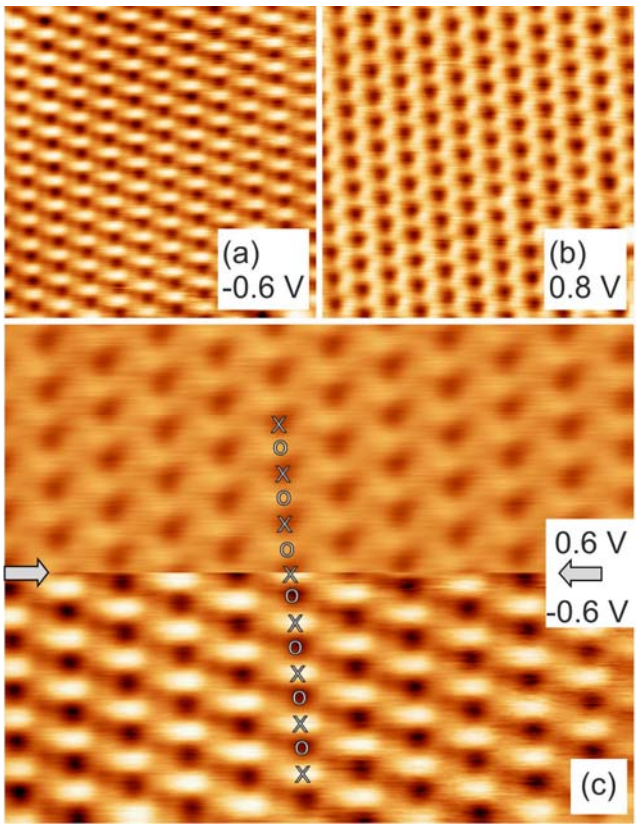

Figure 2

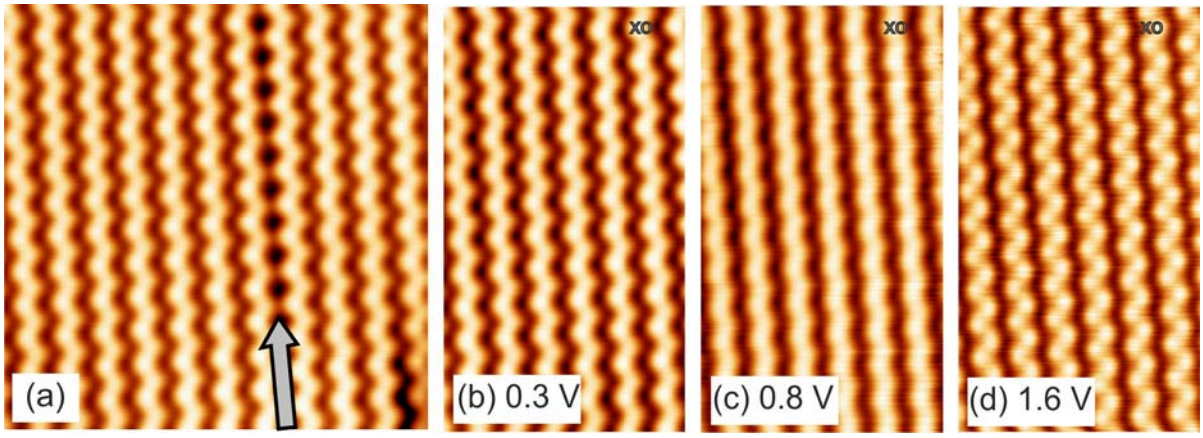

Figure 3

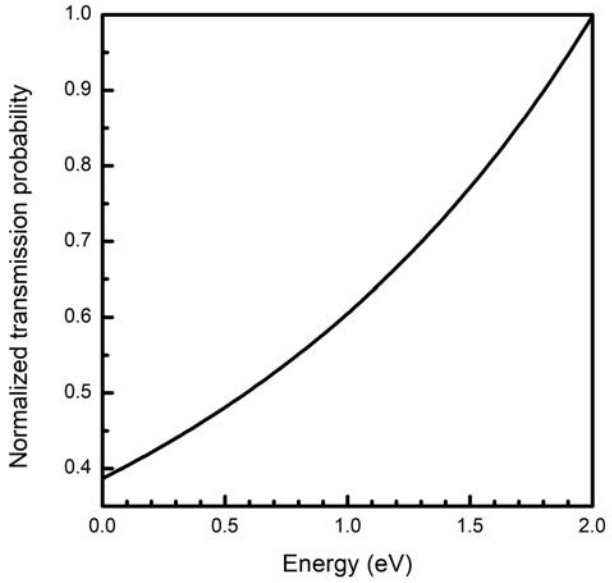
Normalized transmission probability
1.0
0.9
0.8
0.7
0.6
0.5
0.4
0.0
0.5
1.0
1.5
2.0
Energy (eV)

Figure 4

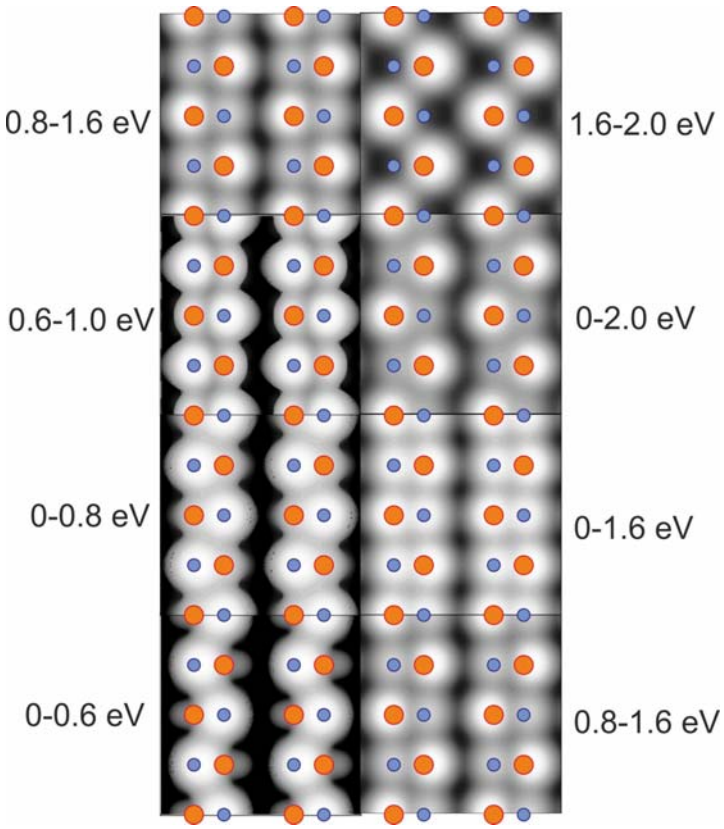

Figure 5

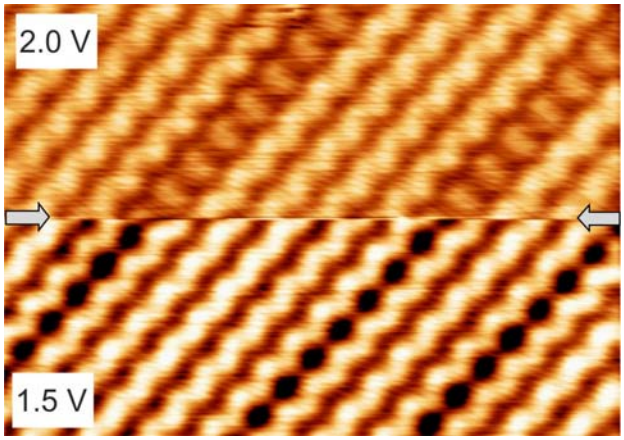

Figure 6

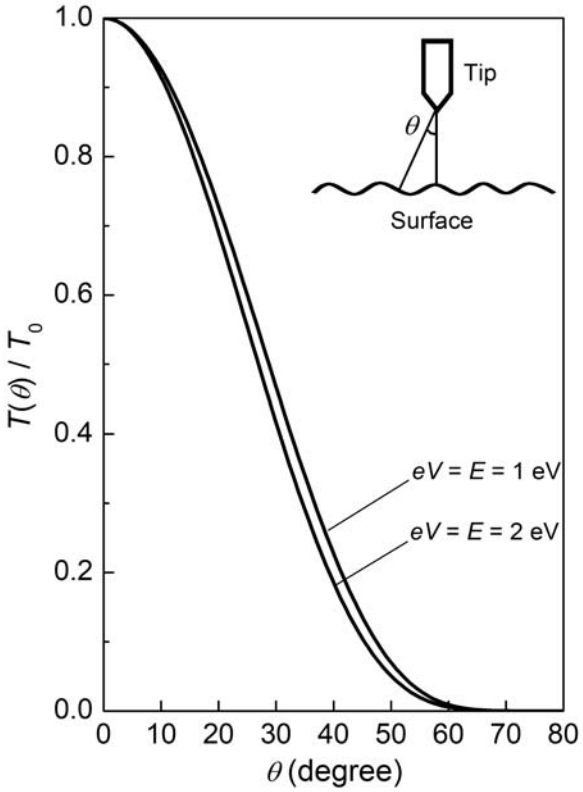
1.0
0.8
0.6
0.4
0.2
0.0
$T(\theta) / T_0$
0
10
20
30
40
50
60
70
80
θ (degree)
Tip
θ
Surface
$eV = E$ = 1 eV
$eV = E$ = 2 eV

Figure 7

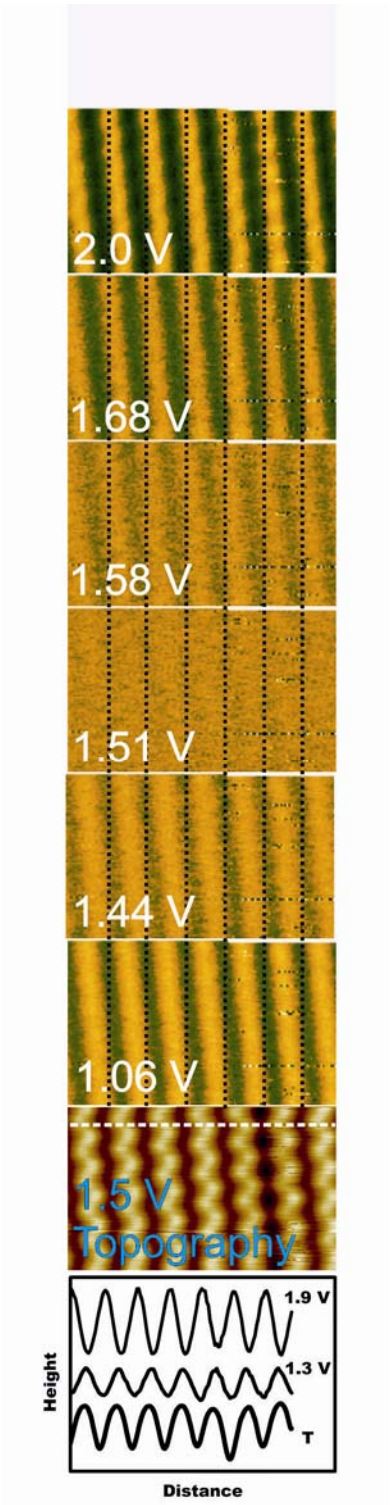
2.0 V
1.68 V
1.58 V
1.51 V
1.44 V
1.06 V
1.5 V
Topography
1.9 V
1.3 V
T
Height
Distance

Figure 8

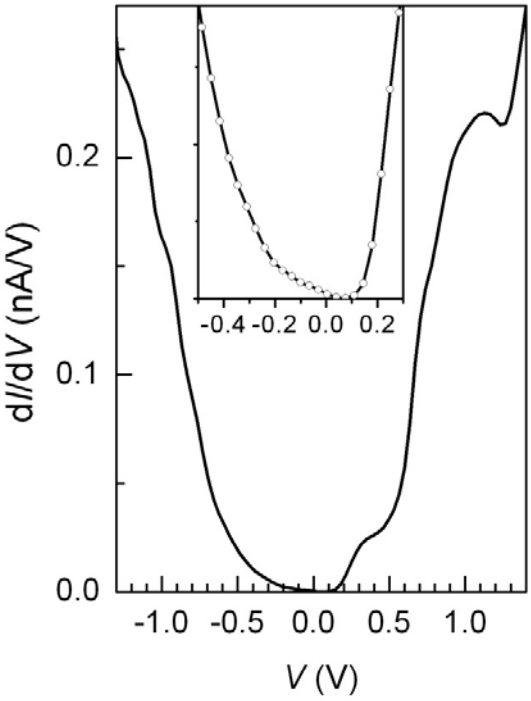

Figure 9

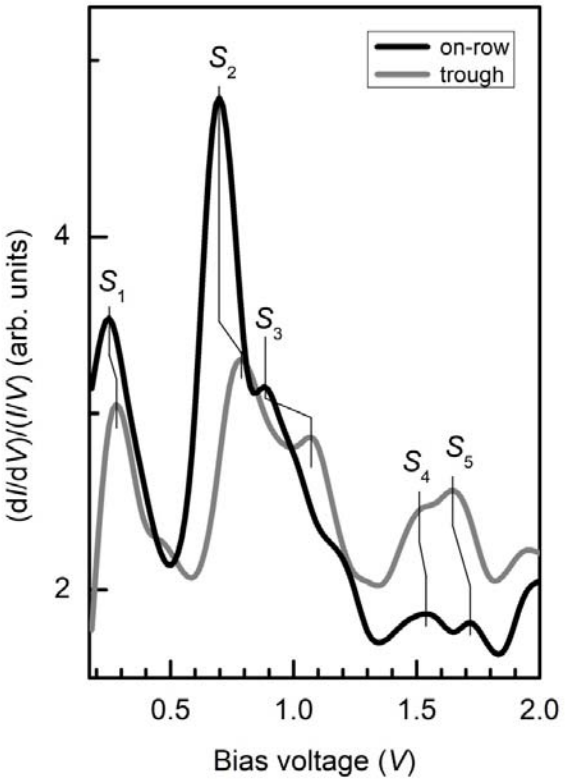
on-row
trough
S_1
S_2
S_3
S_4
S_5
(dI/dV)/(I/V) (arb. units)
4
2
0.5
1.0
1.5
2.0
Bias voltage (V)

Figure 10

.

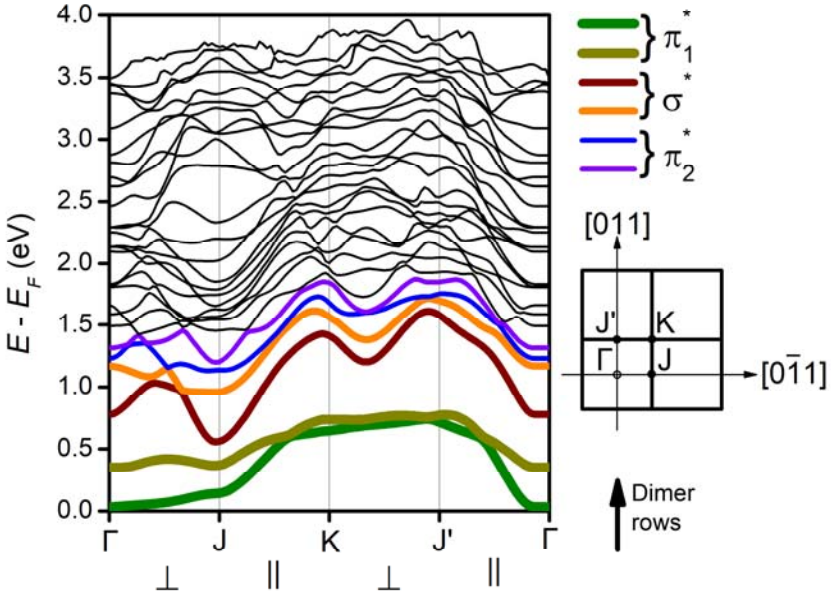
4.0
3.5
3.0
2.5
2.0
1.5
1.0
0.5
0.0
E - E_F (eV)
Γ
J
K
J'
Γ
⊥
||
⊥
||
π*1
σ*
π*2
[011]
J'
K
Γ
J
[0$\bar{1}$1]
Dimer rows

Figure 11